Acta Geotechnica
https://doi.org/10.1007/s11440-024-02354-4

RESEARCH PAPER

Influence of dry density and wetting–drying cycles on the soil–water retention curve of compacted loess: experimental data and modeling

Kangze Yuan[1,2,3] · Wankui Ni[2] · Gabriele Della Vecchia[3] · Xiangfei Lü[2] · Haiman Wang[2] · Yongpeng Nie[2]

Received: 21 December 2021 / Accepted: 16 May 2024

Abstract
In this paper, the EC-5 water sensor and the MPS-6 water potential sensor were used to measure water content and suction, respectively, to investigate the evolution of soil–water retention properties of compacted loess samples prepared at different dry densities and subjected to different numbers of wetting–drying cycles. The water retention data were integrated with a detailed microstructural investigation, including morphological analysis (by scanning electron microscopy) and pore size distribution determination (by nuclear magnetic resonance). The microstructural information obtained shed light on the double porosity nature of compacted loess, allowing the identification of the effects of compaction dry density and wetting–drying cycles at both intra- and inter-aggregate levels. The information obtained at the microstructural scale was used to provide a solid physical basis for the development of a simplified version of the water retention model presented in Della Vecchia et al. (Int J Numer Anal Meth Geomech 39: 702–723, 2015). The model, adapted for engineering application to compacted loess, requires only five parameters to capture the water retention properties of samples characterized by different compaction dry densities and subjected to different numbers of wetting–drying cycles. The comparison between numerical simulations and experimental results, both original and from the literature, shows that only one set of parameters is needed to reproduce the effects of dry density variation, while the variation of only one parameter allows the reproduction of the effects of wetting and drying cycles. With respect to the approaches presented in the literature, where ad hoc calibrations are often used to fit density and wetting–drying cycle effects, the model presented here shows a good compromise between simplicity and predictive capabilities, making it suitable for practical engineering applications.

Keywords Compacted loess · Dry density · Soil–water retention curve · Wetting–drying cycles

1 Introduction

Loess is a special type of sediment formed during the Quaternary period under arid and semiarid climatic conditions [61, 64, 70, 91]. Loess deposits cover 10% of the continents, including Asia, Africa, central and southern Europe, the American Midwest and northern France [14]. Loess is extremely important in northwestern China, mainly in the regions of Shanxi, Gansu and Ningxia, covering about 640,000 km^2 [72]. Loess exists mainly under unsaturated conditions: Knowledge of the water retention curve and its evolution during wetting–drying cycles is therefore fundamental, not only to quantify the water stored in the pores, but also for its effect on

✉ Wankui Ni
niwankui@chd.edu.cn

✉ Gabriele Della Vecchia
gabriele.dellavecchia@polimi.it

[1] State Key Laboratory of Continental Dynamics, Geological Department, Northwest University, Xi'an 710069, People's Republic of China

[2] College of Geological Engineering and Geomatics, Chang'an University, No.126 Yanta Road, Xi'an 710054, Shaanxi, People's Republic of China

[3] Department of Civil and Environmental Engineering, Politecnico di Milano, Piazza Leonardo da Vinci, 32, 20133 Milano, Italy

Published online: 18 June 2024

engineering properties such as shear strength, stiffness, permeability and volume change [23, 25, 40, 77, 96].

The relevant literature clearly demonstrates the important role that the loess microstructure plays in its phenomenological behavior [15, 42, 85, 92], which is also confirmed by recent advances in techniques and methods (see, for example, the works of [43, 47, 83], among others). Ng et al. [56] demonstrated by scanning electron microscopy (SEM) and mercury intrusion porosimetry (MIP) tests that loess is characterized by a double porosity microstructure with two different dominant pore sizes (and both intra- and inter-aggregate pores). When subjected to different hydromechanical loading paths (e.g., stress changes, imbibition, drying), the inter-aggregate pore volume of loess changes significantly, while the intra-aggregate porosity varies slightly, again confirming the dual porosity nature of the internal structure of loess [28, 39, 81].

A large number of experimental studies on the soil–water retention curve of unsaturated loess can be found in the literature [1, 53, 57]. Xie et al. [86] used the filter paper method to determine the soil–water retention curve of loess compacted at different water contents and showed that the curves tend to converge at high suctions. The same method was used by Wang et al. [82] to clarify the role of different dry densities on the retention properties of compacted loess, highlighting that, as for compacted clays, the role of dry density is relevant only in the low suction range. The soil–water retention curves (SWRC) of intact and compacted samples from Lanzhou and Yan'an were determined by Hou et al. [26], which showed that the intact loess has a higher air-occlusion value (AOV) than that of loess compacted to its natural water content, again demonstrating the role of material microstructure. Experimental evidence has been used as the basis for many fitting equations for loess SWRCs. Ye et al. [90] used measurements in the low suction range to predict the entire soil–water retention curves; Li et al. [40] adopted a soil–water interface angle as a fitting coefficient to predict the soil–water retention curve, while grain size distribution was used by Zhang et al. [97] to predict the SWRC of loess characterized by bimodal or multimodal pore size distribution. Although useful for some specific applications, these models are mostly based on empirical phenomenological evidence without linking the water retention properties to the material microstructure: Their range of application is therefore limited.

In recent years, fractal theory has also been increasingly used to relate material microstructure to hydraulic properties of porous media [29, 44, 66]. Russell et al. [67] presented analytical derivations by setting the particle and pore surface areas equal and constant and relating all parameters defining the SWRC to particle and pore geometry information, size distributions, shapes, volumes and surface areas. However, although fractal dimension and air-entry value data based on the MIP test have been used by Tao et al. [73] to make predictions for soil–water retention curves, not all experimental data on loess have been shown to be suitable for the application of fractal theory. To link material microstructure information and hydraulic properties, attempts to link soil–water retention curves and pore size distribution have also been reported in the literature (e.g., [36, 58, 60, 63]). The most commonly used experimental technique to obtain quantitative information on pore size distribution is the MIP (see, e.g., the work of [22, 34, 35], among others). Unfortunately, there are some concerns about performing MIP tests on loess. On the one hand, the mercury used is a heavy metal that is harmful to humans [21, 78]. On the other hand, as a product of weathering, loess is very fragile and its open internal structure could be damaged by mercury intrusion [59, 75], affecting pore topology and leading to inaccurate test results [28, 80, 87]. As an alternative, the nuclear magnetic resonance (NMR) relaxation method has been found to be very effective for nondestructive analysis of the pore size distribution in loess. In fact, NMR has been widely used in geotechnical engineering in recent years [18, 20, 31, 71].

In order to overcome the limitations of current SWRC models in predicting loess retention behavior, this paper presents a comprehensive investigation of the evolution of the soil–water retention curve of compacted loess at different dry densities and subjected to different numbers of wetting–drying cycles, including observation of surface morphology by SEM photomicrographs and pore size distribution obtained by NMR. The range of water contents investigated in this study is between the saturated one and 10%. Indeed, previous research has shown that the water content of loess at different depths typically reaches a minimum in spring, but tends to remain above 10% [88, 93]: wetting–drying cycles resulting from rainfall and evaporation hardly allow the water content of loess to fall below 10%, as also noted by Hou et al. [26] and Li et al. [41]. Phenomenological and microstructural experimental results were interpreted using a double porosity retention framework originally developed for high and medium activity clays [9]. The model incorporates information on intra- and inter-aggregate pore space evolution to reproduce at the continuum scale the different physical processes individuated at the microstructural scale. The low activity of the loess allowed the simplification of the model equations and a significant reduction of the required calibration parameters. Finally, the model was validated against the experimental data on compacted loess presented in this paper and against experimental data on other loess materials from the literature, including both the effects of dry density and the effects of wetting–drying cycles.

2 Materials and methods

2.1 Loess material

The samples investigated were taken from the foundation pit of the Loess Plateau in Yan'an City, China (Fig. 1a). The physical properties of the samples were determined according to the ASTM standard [2]. According to the grain size distribution analysis (Fig. 1b), the content of sand is 10.39%, silt is 78.99% and clay is 10.62%. The mineralogical composition of the loess was analyzed using the X-ray diffraction (XRD) technique (Fig. 1c). XRD is a technique used to analyze the crystalline structure of a material by directing X-rays at a sample and measuring the resulting diffraction patterns [89]. The physical parameters and mineralogical composition of the loess samples are listed in Table 1.

Table 1 Properties of the loess used in this study

Quantity	value
In situ density (kg/m^3)	1.35–1.42
Natural water content (%)	10
Specific gravity	2.71
Plastic limit w_P (%)	16.1
Liquid limit w_L (%)	28.9
Optimal water content w_{opt} (%)	14.1
Maximum dry density (kg/m^3)	1.74
Quartz (%)	45.2
Feldspar (%)	21.0
Calcite (%)	15.5
Chlorite (%)	8.0
Kaolinite (%)	5.8
Illite (%)	4.5

2.2 Preparation of the loess column

The loess samples subjected to wetting–drying cycles were prepared in a column (Fig. 2) at an initial water content of 10% and three different dry densities, namely 1.45, 1.55 and 1.65 kg/m^3, using an apparatus developed in-house [48]. The sample size is 6 cm in height and 30 cm in diameter. The sample was prepared as follows:

(1) First, the original loess was crushed with a wooden hammer until all aggregates were destroyed. The material was then passed through a 2 mm sieve and dried at 105 °C for 8 h to achieve a water content $w_0 \approx 0\%$. An amount of deionized water, calculated from Eq. 1, was then added to the sample using a spray bottle until the target water content (w = 10%) was reached:

$$m_w = \frac{0.01 \cdot (w - w_0)}{1 + 0.01 w_0} \cdot m_0 = 0.01 \cdot w \cdot m_0 \quad (1)$$

where m_w is the mass of deionized water added, m_0 is the mass of the soil sample after drying, w is the target water content (in percent) and w_0 is the initial water content, in this case set equal to 0. The crushed hydrated loess was then sealed tightly with plastic film and placed in a humidor at room temperature for approximately 48 h. A portion of the processed loess was used to check the water content. If the difference between the measured average

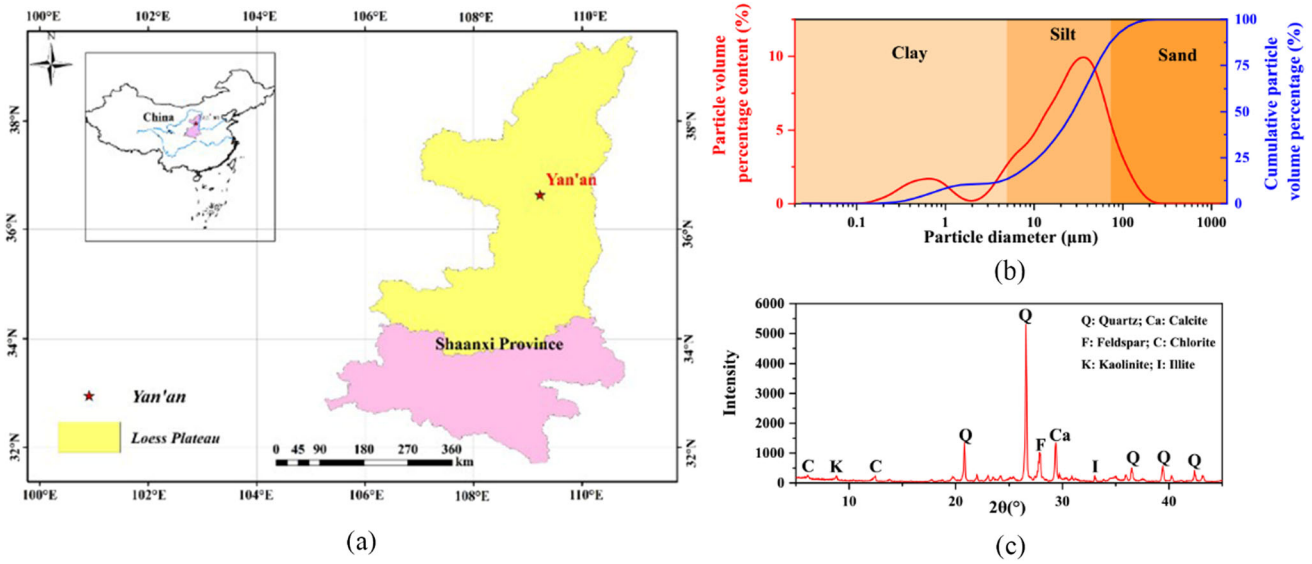

Fig. 1 **a** Occurrence of the Loess Plateau in China and sampling location; **b** Particle size distributions of original loess; **c** XRD pattern of the original loess sample.

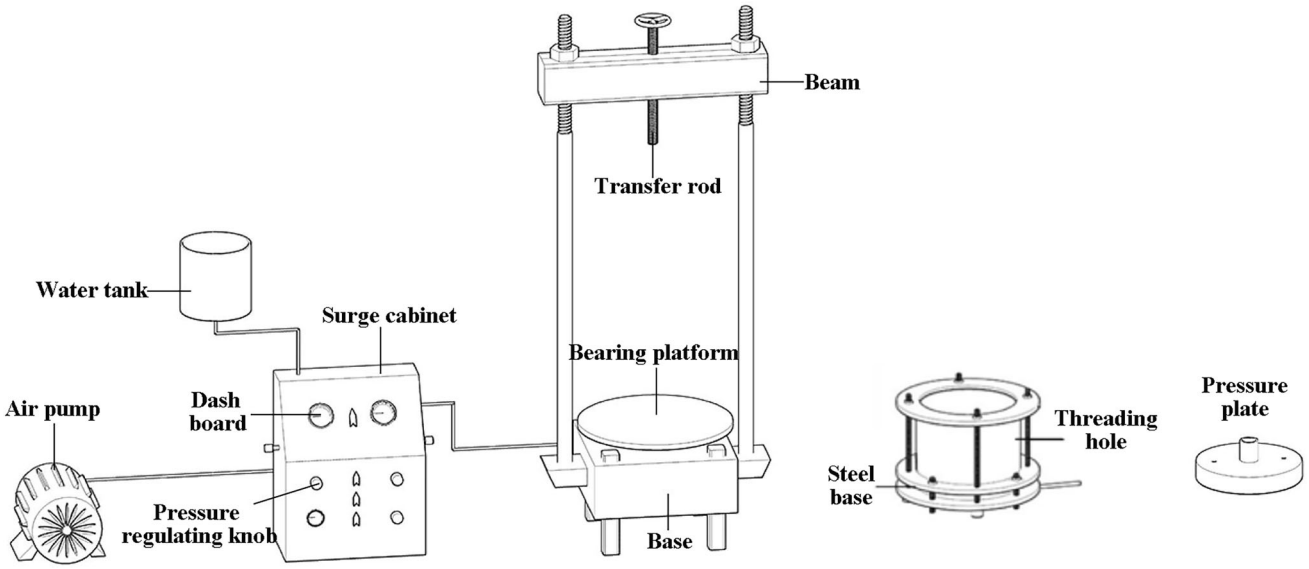

Fig. 2 Schematic of the device for the soil column preparation

water content and the target water content was within ± 0.2%, sample preparation could begin.

(2) Specimens were prepared by compacting the crushed material in three layers. Each layer was statically compacted in the compaction mold by compressing the material at a fixed displacement rate of 1.5 mm/min. To reduce the effect of compaction energy transferred from successive layers, the multilayer with under-compaction method was used to produce the specimens [67]. In this case, each layer is typically compacted to a density lower than the final desired value by a predetermined amount, defined as the percentage of under-compaction U_n, which can be obtained from Eq. 2:

$$U_n = U_{ni} - \left[\frac{(U_{ni} - U_{nt})}{n_t - 1} \times (n - 1)\right] \quad (2)$$

where U_n is the percentage of under-compaction in the layer considered, U_{ni} is the percentage of under-compaction selected for the first layer, U_{nt} is the percentage of under-compactions selected for the last layer (usually zero), n is the number of layers considered, n_t is the total number of layers. In this study, the value of U_{ni} was set equal to 15%. Once U_n has been selected for layer 1, the appropriate mass of soil for layer 1 is poured into the device (i.e., the mass of soil is the same for each layer) and then compacted to the thickness of the soil layer corresponding to the specific percentage of under-compaction (see [69] for details).

(3) After compacting the first layer, the soil surface was carefully leveled. Since the water potential and water sensors had to be placed in the middle of the second layer, half the mass of loess for the second layer was weighed, lightly compacted in the soil column and leveled. An MPS-6 water potential sensor (Fig. 3a) for measuring suction in the range 9–100,000 kPa [49, 79] and an EC-5 water sensor (Fig. 3b) for measuring the degree of saturation from 0 to 100% were then placed in contact with the top of the compacted soil (Fig. 3d) [68]. After placing the sensors, another half mass of loess was added for the second layer and smoothed. The compaction method was the same as in step (2);

(4) The third layer was prepared as the first one, as discussed in step (2);

(5) Once the sample was prepared, it was placed in the laboratory environment and weighed periodically. It was found that the total mass remained essentially constant, so the water content of the sample remained at the target water content (10%). The sample was then sealed with a film to prevent water evaporation. The EM50 data collector (Fig. 3c) was used to record the suction and water content data.

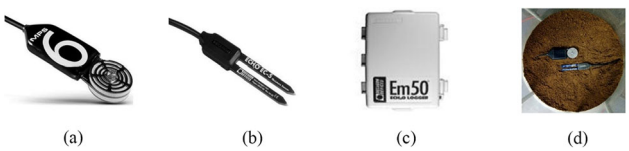

Fig. 3 Experimental equipment (**a**. MPS-6 water potential sensor; **b**. EC-5 water sensor; **c**. EM50 data collector; **d**. Sensor placement)

2.3 Wetting–drying cycles and soil–water retention curve determination

The experimental procedure for performing the wetting–drying cycles and SWRC determination is shown in Fig. 4. The whole test was performed in a constant temperature environment, corresponding to 22 ± 1 °C. After the loess column was prepared as described in Sect. 2.2, a 2 cm layer of quartz sand was placed at the top of the loess column to reduce damage to the top surface. To reduce the influence of sensor hysteresis, the wetting–drying process was performed at a relatively slow rate, allowing the sensor to accurately measure the water content and suction values. A water head of 2 cm was applied to the quartz sand layer to induce wetting of the loess columns. The 2 cm water head was maintained by a continuous supply of water. Some small holes at the bottom of the experimental apparatus and the presence of filter paper allowed water to drain at the bottom of the column. Due to the difference in hydraulic head between the top and bottom of the column, water began to flow into the sample, increasing its water content. The EM50 data collector operated continuously during the wetting–drying process, recording the changes in water content and suction. As the water content of the sample approached saturation, some water would flow out of the tube (red one). When the water infiltration rate in the tube remained stable for at least two hours, along with the measured values of water content and suction, the wetting process was stopped and the loess column was considered 'saturated.' The water content and suction measured at the center of the sample at this stage are then assumed to provide information on the main wetting branch (from 10% water content to saturation) of the loess water retention curve. This assumption is based on several experimental data showing that the hysteresis of the water retention curve is almost negligible at low water contents (see, e.g., Xie et al. [86]; Liang et al. [46]; Li et al. [38]). The EC-5 water sensor and MPS-6 water potential sensor can provide direct data on water content and suction, providing more direct and accurate experimental information compared to the results of the filter paper method, which requires calibration and further calculations to obtain suction values [17].

After the complete saturation of the soil column, the drying stage follows. The loess column was subjected to air-drying in the laboratory environment. During drying, the weight of the sample was measured. Specimens were weighed periodically until the total mass remained constant for 2 weeks, during which time the water content and suction values also stabilized. The water content at the end of the drying stage is approximately 10%. Comparison of water content data from both weighing and sensor methods was performed to ensure data reliability through redundancy and cross-verification. The height of the samples was also measured using calipers during the wetting–drying cycles: the height was found to change slightly, as in Mu et al. [52], and thus the total volume change of the samples during the water retention test was neglected. This is consistent with the mineralogical composition of the loess (mostly composed of silt) [47] and the presence of only small amounts of non-expansive clay minerals, i.e., kaolinite and illite (see Table 1). The above steps were repeated until three complete wetting–drying cycle tests were performed. Finally, the experimental data of the time evolution of water content and suction in the center of the specimen were exported from the data collector.

2.4 Microstructural characterization

Samples after different number of wetting–drying cycles were carefully selected for microstructural characterization. Prior to SEM testing, cuboids of 1 × 1 × 2 cm

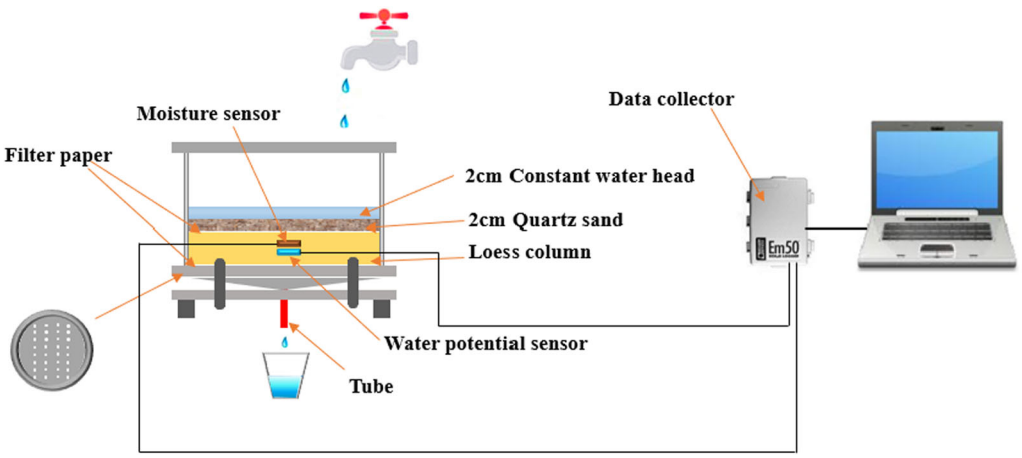

Fig. 4 Schematic of the wetting–drying experimental apparatus

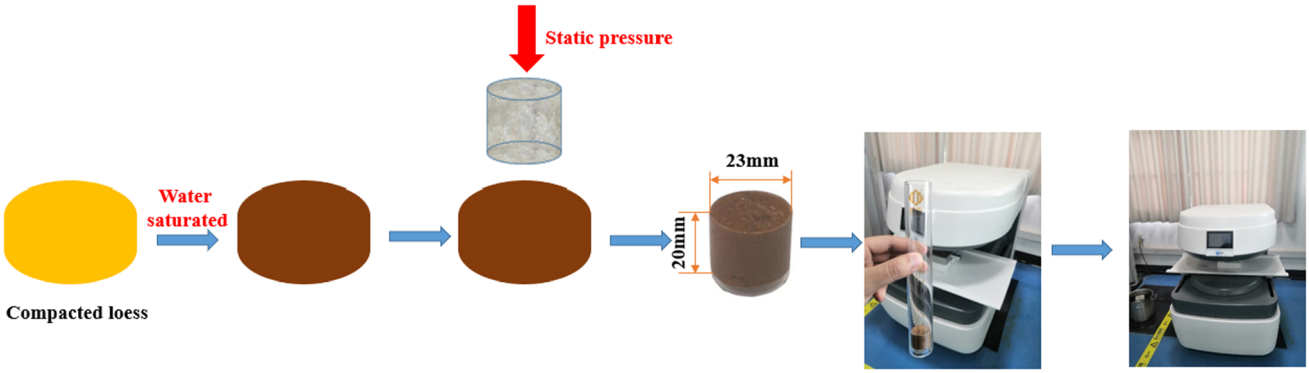

Fig. 5 NMR sample preparation and test procedure

(length × width × height) were cut from the central part of the loess samples. Appropriate sample drying methods should be used to minimize the impact of preparation work [65], but air-drying has been widely used in soil science because of its cheapness and simplicity [3, 50, 76]. Samples were air-dried in the laboratory environment, allowing the soil to slowly lose water (e.g., [7]). This process took about 30 days. Careful measurements were taken to verify the change in volume of the samples due to air-drying, which was found to be less than 1%. Due to the negligible shrinkage induced by air-drying, the effect on the microstructure of the loess material was considered negligible, as in Ma et al. [50]. Half of the rod was then attached to the shooting pad for sputtering with platinum (Pt) in a sputtering ion apparatus using electron-conducting tape, without disturbing the fracture plane. A FEI MLA650F SEM was used to record the microstructure images of all specimens.

Geophysical NMR methods, specifically implemented with the MacroMR12-150H-1 instrument, were used to analyze the pore size distributions of the loess samples. The theoretical basis for geophysical NMR methods, as documented in the literature [6, 27], derives from the inherent magnetic dipole moment of H protons within water molecules, a consequence of their nuclear spin angular momentum. In the presence of a static magnetic field, denoted B_0, the nuclear spins align with the magnetic field, resulting in an additional macroscopic magnetization (M) oriented parallel to B_0. Conventional NMR techniques use artificial magnetic fields in the laboratory to induce a magnetization M whose equilibrium magnitude is proportional to the amount of H protons in the observed volume, which represents the volume of water in the sample. When the excitation magnetic field oscillates at precisely the precession frequency of the spins (i.e., the Larmor frequency), M is forced away from its equilibrium position. When the excitation is removed, M processes at the Larmor frequency around B_0 and returns to its equilibrium state through an energy exchange between the nuclear spins and their environment. The subsequent relaxation of M is studied, showing two distinct forms: longitudinal relaxation (T_1), which occurs parallel to B_0, and transverse relaxation (T_2), which occurs perpendicular to B_0. In porous media, the relaxing NMR signal typically exhibits a multiexponential decay, starting from an initial signal amplitude that is linearly dependent on the amount of protons in the entire pore space, which is indicative of the water content. Consequently, the signal amplitude serves as an indicator of the presence of fluid in the pores and is correlated with the characteristic pore abundance when the pores are saturated. In particular, the NMR intensity is usually expressed in arbitrary units (a.u.), as illustrated in previous works, e.g., [16]. In particular, the relaxation time T_2 is the transverse relaxation time of the pore water between the loess particles as measured by a Carr-Purcell-Meiboom-Gill (CPMG) sequence. It is a measure of the rate at which the precession of hydrogen nuclei in the formation of pore water gradually decays in the presence of an inhomogeneous magnetic field, and can be used to calculate the pore size distributions of loess samples. From the above description, it can be concluded that pore water between loess particles is a necessary condition for this measurement. Therefore, the compacted loess samples from the cutting ring were saturated under vacuum conditions [86] and fixed in a specially made quartz tube (diameter 23 mm × height 20 mm). This quartz tube containing the loess sample was then placed in the test tube to obtain the T_2 curve. A schematic of this procedure is shown in Fig. 5. For water-saturated loess samples, T_2 can be obtained from Eq. 3, based on the NMR relaxation mechanisms [4]:

$$\frac{1}{T_2}=\frac{1}{T_{2B}}+\frac{1}{T_{2S}}+\frac{1}{T_{2D}} \tag{3}$$

where T_{2B} is the bulk water relaxation time, T_{2S} is the surface-enhanced relaxation time at the pore walls and T_{2D} is the diffusion relaxation time, which accounts for the transverse relaxation in an inhomogeneous magnetic field.

For water, T_{2B} is much larger than T_{2S} and T_{2D}, so the effect of T_{2B} on T_2 can be ignored. For pore water in porous loess, T_2 of pore water is then directly related to the internal pore structure of the loess, as

$$\frac{1}{T_2} = \frac{1}{T_{2S}} = \rho\frac{S}{V} = \rho\frac{\alpha}{r} \tag{4}$$

where ρ (expressed in general in μm/s) is the surface relaxivity coefficient, characterizing the magnetic interactions at the water-loess particles interface, and *S/V* is the ratio between the pore surface area S to the pore water volume V. The ratio *S/V* is proportional to the reciprocal of pore radius r, expressed as $\frac{\alpha}{r}$. The geometry factor α in Eq. 4 depends on the pore shape: for example, $\alpha = 1$ for planar pores, $\alpha = 2$ for cylindrical pores and $\alpha = 3$ for spherical pores. In this study, we assume that the pore structure is made of cylindrical pores. Hence, Eq. 4 finally reads:

$$\frac{1}{T_2} = \rho\frac{\alpha}{r} = \rho\frac{2}{r} \tag{5}$$

or

$$T_2 = \frac{1}{2\rho}r \tag{6}$$

To determine the surface relaxivity coefficient ρ, the widely accepted NMR-permeability equation, known as Schlumberger-Doll Research (SDR) equation developed by Kleinberg et al. [32], is used. The SDR equation links the surface relaxivity coefficient (ρ) to soil saturated permeability k_s as

$$k_s = C\phi^4 T_{2LM}^2 \tag{7}$$

being the constant C expected to coincide with the square of the surface relaxivity coefficient, ϕ the porosity and T_{2LM} the geometric mean value of the T_2 distribution, obtained using the Statistical Product and Service Solutions (SPSS) software [30].

This dependence of k_s on ρ may be written as

$$k_s = \rho^2\phi^4 T_{2LM}^2 \tag{8}$$

leading to

$$\rho = \sqrt{\frac{k_s}{\phi^4 T_{2LM}^2}} \tag{9}$$

For the three samples corresponding to the dry densities of 1.45, 1.55 and 1.65 kg/m^3, the saturated permeability (k_s) of the loess was equal to 9.13×10^{-14}, 4.36×10^{-14} and 1.93×10^{-14} m^2, respectively, as obtained in [37]. As for the mean geometric value of the T_{2LM} distribution, the values obtained are 0.5232, 0.4532 and 0.3935 ms, respectively. By using these values in Eq. 9, a value of ρ= 2.65 μm/ms is obtained for the sample with a dry density 1.45 kg/m^3, while the ρ values for the samples with dry density of 1.55 and 1.65 kg/m^3 are 2.49 and 2.27 μm/ms, respectively. According to Eq. 9, the surface relaxation coefficient should vary with ϕ and k_s. Strictly speaking, this means that a saturated permeability measurement should be required for each test. However, according to the relevant scientific literature, the need to perform saturated permeability tests to obtain ρ before each test is often ignored, based on the evidence that the major contribution to the surface relaxation coefficient is due to the paramagnetic impurities on the surface of the grains, which interact with hydrogen nuclei and impose an additional relaxation [4]. This contribution is considered to be constant for a given soil at a given compaction density, depending on the specific combination of mineral grains [37, 75].

3 Result and discussion

3.1 Evolution of soil–water retention curve with dry density and wetting–drying cycles

The main wetting branches of the soil–water retention curves of compacted loess with different dry densities are shown in Fig. 6a. As expected, the highest air-occlusion value is that corresponding to the highest density, while the lowest is that corresponding to the lowest density. The air-occlusion value is the suction value below which the gas phase is no longer continuous in the pore space during a wetting process and plays the same role as the air-entry value for the main drying path of a water retention curve (see, e.g., [62]). The variation of the air-occlusion values in the retention properties at near saturation conditions implies an intersection of the wetting curves at a suction of near 20 kPa. This seems to be consistent with the pore size distribution for the three as-compacted samples shown in Fig. 6b: for a pore size diameter greater than 15 μm (corresponding to a suction of about 20 kPa according to the Laplace equation), the NMR signal intensity is greater at lower densities. The difference in retention capacity at low suction is therefore related to the presence of a greater number of large diameter pores in the lowest density sample. Due to the presence of these macropores, the low density sample is characterized by a higher water content and a higher water uptake rate at suctions lower than 20 kPa. In agreement with the water retention curve data, the NMR intensity curves also cross for pore size diameters below 20 μm. For suctions higher than 200 kPa, the effect of initial dry density begins to be negligible in the retention plane. At high suctions, the water content in the compacted loess is low and the water is mainly distributed in the

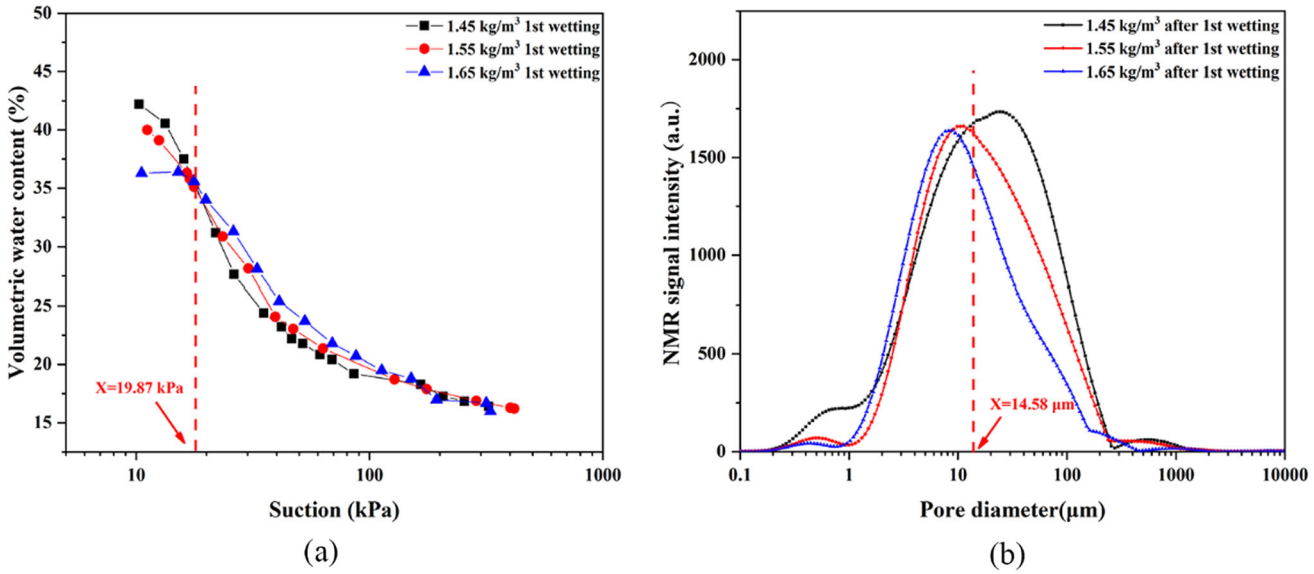

Fig. 6 **a** Soil–water retention curves at different dry densities along the first wetting path; **b** NMR signal intensity for as-compacted specimens

smallest pores, which have already been shown to be hardly affected by dry density (see, e.g., [80]). This is in agreement with a number of experimental results obtained for compacted clays (see, e.g., [13, 52, 62]). Drying curve data are not shown because the drying stage was carried out at such a high rate that it was not possible to guarantee uniformity of water distribution inside the sample during the drying process itself. Uniformity of water distribution and suction is guaranteed only after the entire drying process has been completed, i.e., when the total mass has remained constant for 2 weeks, during which time the water content and suction values have also stabilized. Accordingly, only the data from the wetting path can be considered reliable for representing the wetting branch of the material's water retention curve, while the drying path is used only as part of the wetting–drying cycle.

It is worth noting that recent literature [94] has highlighted the role of the so-called 'rain-drop' and 'ink-bottle' effects on the hysteresis of the SWRC, showing that a better relationship between the pore size distribution and the retention curve is obtained along the main drying path. According to these limitations, the pore size distribution has not been used in this work to obtain the water retention curve quantitatively, but as a tool from which qualitative information is obtained for modeling purposes, as in Romero et al. [62] and Della Vecchia et al. [11].

The wetting branch of the soil–water retention curves of compacted loess previously subjected to one, two and three repeated wetting–drying cycles is shown in Fig. 7. Figure 7a refers to loess samples compacted at a dry density of 1.45 kg/m^3, Fig. 7b refers to samples compacted at 1.55 kg/m^3 and Fig. 7c refers to samples compacted at 1.65 kg/m^3. For each compacted dry density, the volumetric water content at saturation (coincident with the porosity) increases with the number of wetting–drying cycles. For the loess specimen compacted at 1.45 kg/m^3, the increase in saturated volumetric water content from cycle 1 to cycle 2 is 5.5%, and from cycle 2 to cycle 3, it is 4.6%. A similar increase in the saturated volumetric water content (about 5.7% from cycle 1 to cycle 2 and 5.3% from cycle 2 to cycle 3) is obtained for the loess sample compacted at 1.55 kg/m^3 and for the loess sample compacted at 1.65 kg/m^3. As expected, the effect on material porosity decreases with increasing number of cycles increases [84]. It is interesting to note that although the total volume change of the samples during the water retention test is negligible, the saturated volumetric water content (i.e., porosity) of the loess changes significantly with increasing wetting–drying cycles. This is due to the fact that the wetting process in loess leads to the dissolution of soluble salts and soluble cementitious materials in water (see, e.g., [80]). In fact, porosity is defined as the ratio between the volume of the voids and the total volume: if the total volume is constant, the observed change in porosity is related to the change in the volume of the voids, which is equal (and opposite in sign) to the change in the volume of the solids [33]. Significant differences in retention properties occur mostly at low suctions, where the largest voids and macrostructural changes occur during wetting–drying cycles [37]. Conversely, at high suction the soil–water retention curves of compacted loess with different dry densities tend to coincide.

Figure 8a shows a comparison between the wetting branches of the soil–water retention curves after three wetting–drying cycles of the loess samples compacted at different dry densities. Compared to the retention curves

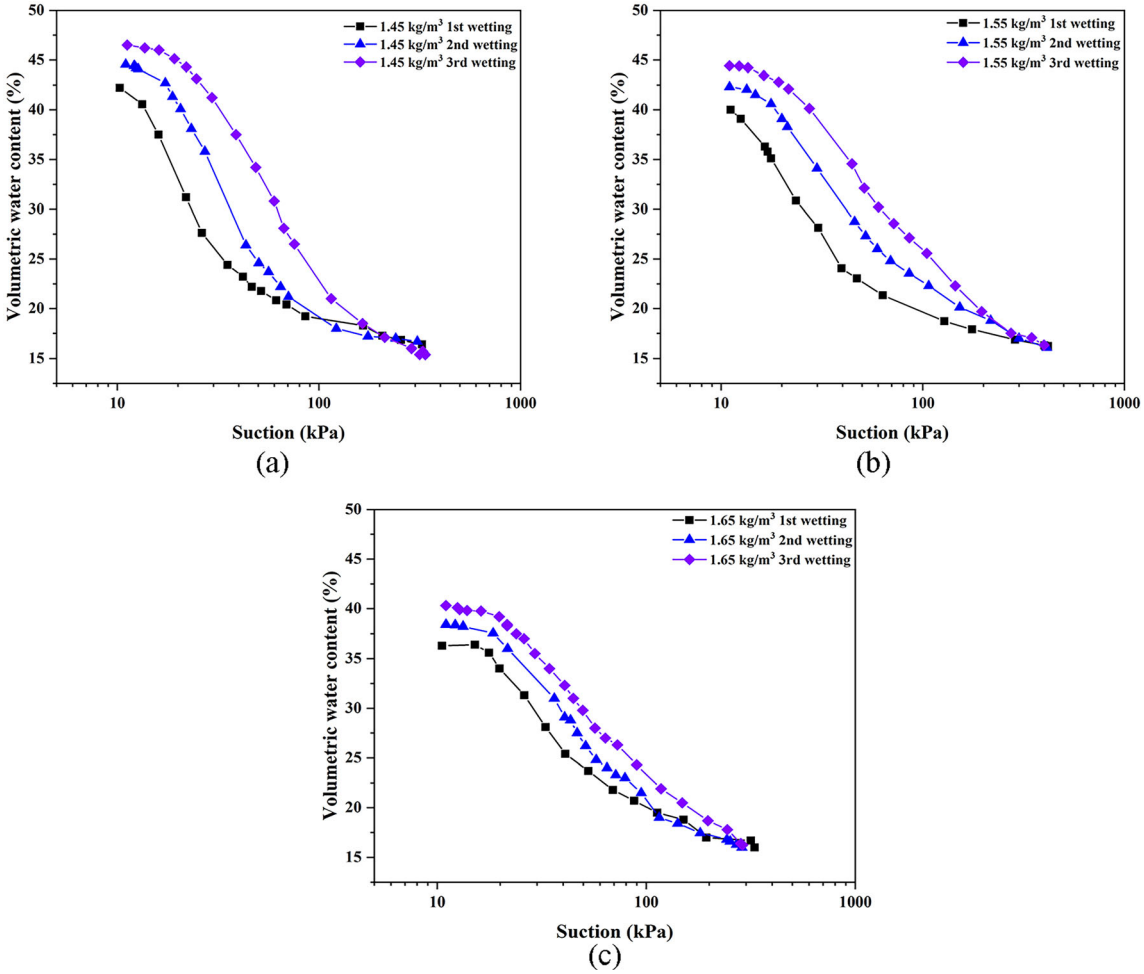

Fig. 7 Soil–water retention curves after wetting–drying cycles (**a**: ρ_d = 1.45 kg/m^3; **b**: ρ_d = 1.55 kg/m^3; **c**: ρ_d = 1.65 kg/m^3)

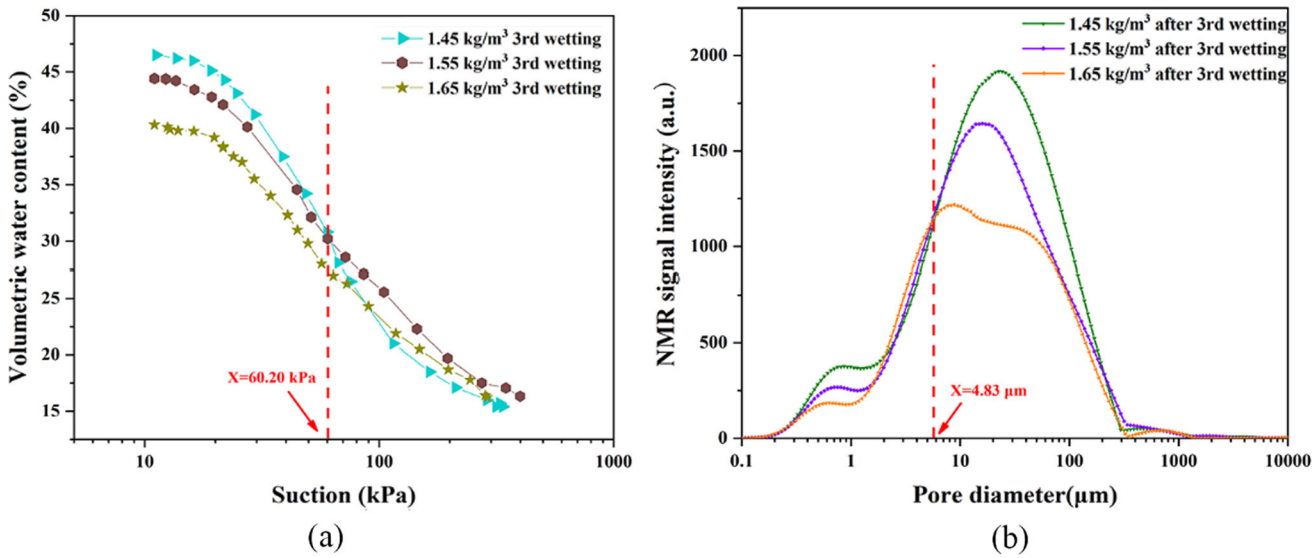

Fig 8 **a** Soil–water retention curves measured along the third wetting path at different compaction dry densities; **b** NMR signal intensity curves measured after the third wetting.

measured along the first wetting process, the effect of dry density seems to be more relevant. The soil–water retention curves of loess compacted at different dry densities still cross after wetting and drying cycles, but the suction at which the curves cross increases. Samples with dry densities of 1.45 and 1.55 kg/m^3 cross at a suction of 60 kPa, while samples with dry densities of 1.45 and 1.65 kg/m^3 cross at a slightly higher suction, about 90 kPa. Despite the slight difference in the crossing suction data, the overall picture appears to be consistent with the results of the NMR pore size distributions of the three compacted samples after three wetting cycles. In fact, the three NMR curves cross at a pore diameter of about 4.8 μm, corresponding to a suction of about 60 kPa according to Laplace's equation. It is interesting to compare Figs. 6b and 8b, where the change in the pore distribution curves with wetting–drying cycle is evident for different dry densities of compacted loess with the assumption of a constant overall volume of the sample (Sect. 2.3). This is because the wetting process leads to the dissolution of soluble salts and soluble cementitious materials in water [80]. Due to some small holes at the bottom of the experimental apparatus (Fig. 4), the mixed solution (containing both soluble salts and soluble cementitious materials) was allowed to drain from the bottom of the column through the tube (colored in red in Fig. 4). Thus, the total volume of the sample does not change, but the total pore volume of the sample (and thus the porosity) is affected. This also explains the increase in saturated volumetric water content in the soil–water retention curves for different dry densities of compacted loess in Fig. 7.

3.2 An insight into microstructural changes

The morphology of the skeleton particles is compared at 1000 × magnification for each dry density before and after wetting–drying cycles (Fig. 9). Not only are aggregates and inter-aggregate pore space visible in the SEM image, but the presence of intra-aggregate pores is also highlighted, suggesting the possibility of adopting a double porosity framework for interpreting material behavior. A structural level is thus identified by the aggregates and the pores within them, also called 'micropores' or 'intra-aggregate voids.' Conversely, the macrostructure is identified as the pore network consisting of the voids between the aggregates, also known as 'macropores' or 'inter-aggregate voids' [54]. Figure 9a shows the surface morphology at a dry density of 1.45 kg/m^3: The contacts between the aggregates are dense and there are many inter-aggregate pores. For compacted loess with a dry density of 1.55 kg/m^3 (Fig. 9c), the contact between the aggregates in the loess is closer and the inter-aggregate pores in the loess structure are significantly reduced. The inter-aggregate voids are further reduced for the 1.65 kg/m^3 dry density sample (Fig. 9e). After three wetting–drying cycles, the structure of the compacted loess becomes looser and more inter-aggregate pores are formed due to the loss of soluble salts and cementing materials [89]. In order to use NMR to obtain a quantitative insight into the evolution of intra- and inter-aggregate porosity of compacted loess at different compaction states and along different wetting–drying cycles, a criterion to distinguish between intra- and inter-aggregate porosity is required (e.g., [5, 62, 95]). Figure 10 shows the cumulative NMR intensity curves of compacted loess at different dry densities and wetting–drying cycles. The pore distribution appears as unimodal, due to the partial superimposition in terms of pore size of intra- and inter-aggregate pores in the compacted loess. As discussed earlier, wetting–drying cycles and dry density have little influence on the retention curve in the high suction region: the pore volume belonging to this retention region can thus be assumed to coincide, to a first approximation, with the intra-aggregate pore volume. Figure 10 also shows that the cumulative NMR intensity curves of compacted loess with different dry densities and wetting–drying cycles coincide when the pore size is less than 6.9 μm (as proposed in [92]). For pore sizes larger than 6.9 μm, the differences between the cumulative NMR curves begin to change significantly. Therefore, the discriminating pore size between intra-aggregate and inter-aggregate porosity was set constant and equal to 6.9 μm. The choice of a constant discriminating pore size between larger and smaller voids during wetting and drying cycles is consistent with Hasdari and Russell [24].

To quantify the fabric evolution of compacted loess due to density changes and after wetting–drying cycles, NMR signal intensity data are used, relying on the fact that the cumulative NMR intensity of saturated samples is proportional to pore volume [37]. Since e_{tot} is the total void ratio of the samples obtained by water content measurements at the end of the wetting process, the changes in intra- and inter-aggregate void ratio can be evaluated according to the changes in cumulative NMR intensity. The intra-aggregate void ratio e_m and the inter-aggregate void ratio e_M are defined here as

$$e_m = e_{\text{tot}} \cdot \frac{T_m}{T_{tol}} \tag{10}$$

$$e_M = e_{\text{tot}} \cdot \frac{T_M}{T_{tol}} \tag{11}$$

where T_m is the cumulative NMR intensity up to the discriminating diameter of 6.9 μm and T_M is the cumulative NMR intensity corresponding to pores with diameter greater than 6.9 μm, and T_{tol} is the total cumulative NMR intensity of loess samples.

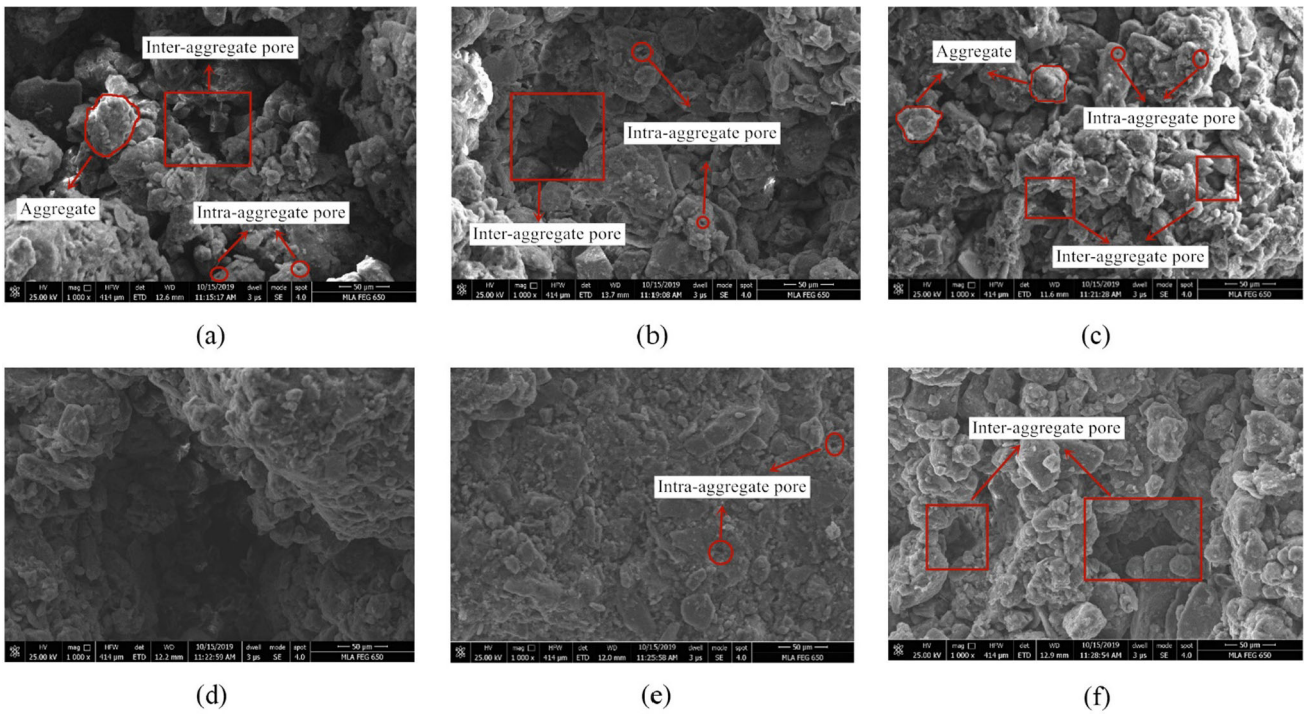

Fig. 9 SEM photomicrographs showing the surface morphology of compacted loess before and after wetting–drying cycles. (**a**: ρ_d = 1.45 kg/m^3 no cycles; **b**: ρ_d = 1.45 kg/m^3 3 cycles; **c**: ρ_d = 1.55 kg/m^3 no cycles; **d**: ρ_d = 1.55 kg/m^3 3 cycles; **e**: ρ_d = 1.65 kg/m^3 no cycles; **f**: ρ_d = 1.65 kg/m^3 3 cycles)

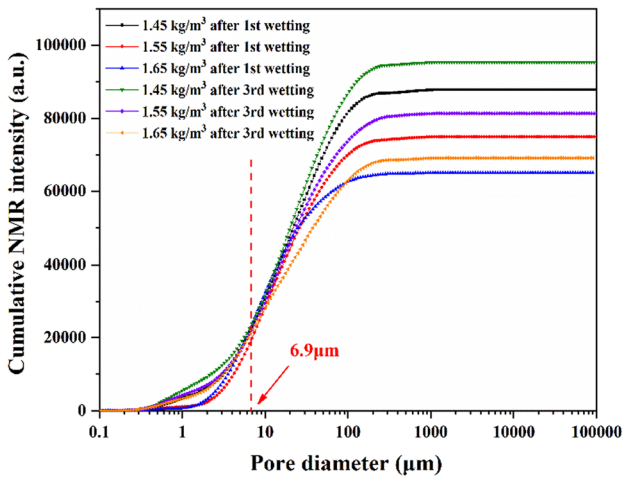

Fig. 10 Cumulative NMR intensity curves of compacted loess

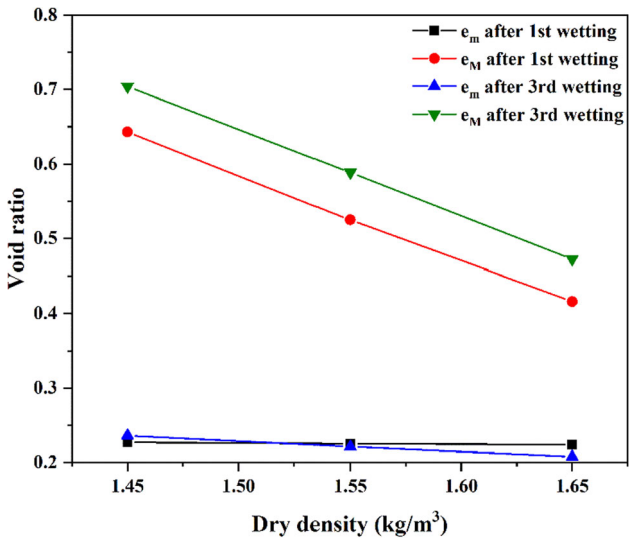

Fig. 11 Evolution of e_m and e_M as a function of dry density after different numbers of wetting–drying cycles

Figure 11 shows the evolution of e_m and e_M with dry density for different wetting–drying cycles. As the dry density increases, e_M decreases gradually, while e_m changes slightly. The rate of decrease of e_M with dry density is the same before and after the wetting–drying cycles: wetting–drying cycles therefore seem to have basically the same influence on e_M regardless of the compacted dry density. As far as e_m is concerned, there is no particular influence of either dry density or wetting–drying cycles.

4 Modeling the dry density and wetting–drying effects on compacted loess

According to the experimental data collected in this work and in the literature (e.g., [28, 82]), the hydraulic behavior of compacted loess can be interpreted in the framework of double porosity media. Accordingly, the modeling

framework for compacted clays proposed by Della Vecchia et al. [9] is used here to propose a water retention model capable of reproducing the effect of compaction density and wetting–drying cycles on the retention properties of compacted loess. According to the double porosity framework, the water ratio e_w (volume of water over the volume of solids) of a double porosity medium can be split into two contributions, one due to water belonging to intra-aggregate pores and one due to water stored in inter-aggregate pores.

$$e_w = e_m S_{\mathrm{rm}} + e_M S_{\mathrm{rM}} \tag{12}$$

where e_m is the void ratio of the microstructure (volume of intra-aggregate voids over the solid volume), e_M is the void ratio of the macrostructure (volume of inter-aggregate voids over the solid volume), S_{rm} is the degree of saturation of micro-voids (volume of water in the intra-aggregate voids over the intra-aggregate void volume) and S_{rM} is the degree of saturation of macrovoids (volume of water in the inter-aggregate voids over the inter-aggregate void volume). Each water retention domain can be modeled, as a first approximation, by means of a van Genuchten equation, i.e.,

$$S_{\mathrm{rm}} = \frac{V_{\mathrm{wm}}}{V_{\mathrm{vm}}} = \left[\frac{1}{1+(\alpha_m \psi)^{n_m}}\right]^{m_m} \tag{13}$$

$$S_{\mathrm{rM}} = \frac{V_{\mathrm{wM}}}{V_{\mathrm{vM}}} = \left[\frac{1}{1+(\alpha_M \psi)^{n_M}}\right]^{m_M} \tag{14}$$

where n_m, m_m, α_m and n_M, m_M, α_M are the van Genuchten material parameters for the intra- and inter-aggregate retention domains, respectively, and ψ is suction.

4.1 Dry density effects

The introduced model has been fruitfully used to reproduce the retention behavior of compacted clays, due to its ability to account for the evolution of clay microstructure, i.e., considering the different roles of e_m and e_M. The evolution of the intra-aggregate void ratio is related to clay activity, and several proposals have been made to reproduce aggregate deformation, introducing a relationship between the evolution of the intra-aggregate void ratio and water content [12, 62], suction [8] or pore fluid salinity [9, 55]. In this case, according to the experimental evidence at the microstructural scale presented in Fig. 11, the role of evolving aggregates is neglected and the intra-aggregate void ratio has been set constant and equal to e_{m0}= 0.23. Indirectly, the deformation of the aggregates also affects the macropore volume, being $e_M = e - e_{m0}$.

Besides the direct effects on pore water distribution, intra- and inter-aggregate void ratios also affect the AOVs of the relevant domains. For instance, in Della Vecchia et al. [9] the evolution of α_m and α_M was set as:

$$\frac{1}{\alpha_m} = \alpha_1^m \exp\left(-\alpha_2^m e_m\right) \tag{15}$$

$$\frac{1}{\alpha_M} = \alpha_1^M \exp\left(-\alpha_2^M e_M\right) \tag{16}$$

where α_1^m, α_2^m and α_1^M, α_2^M are model parameters. This approach has been found to be useful in reproducing the role of void ratio changes under hydromechanical loading in compacted clays, including Boom clay [62], London clay [51], Hong Kong clay [45], Febex bentonite and MX-80 bentonite [13]. However, simplifications are possible for low activity materials such as loess. Due to the negligible change of aggregate size, the dependence of α_m on e_m can be neglected (i.e., Equation 15 is no longer needed) and α_m can be considered as a material parameter. In addition, a link between n_m and m_m can be imposed, as:

$$m_m = 1 - \frac{1}{n_m} \tag{17}$$

Thus, only two parameters are needed to describe the water retention curve in the high suction range. Finally, for the low suction part of the curve, Eq. (16) can be simplified by setting $\alpha_2{}^{\mathrm{M}} = 1$. The evolution of parameter α_M thus now reads:

$$\frac{1}{\alpha_M} = \alpha_1^M \exp(-e_M) \tag{18}$$

The approach was first used to reproduce the water retention curves of Yan'an City compacted loess at different dry densities. The experimental data presented in Fig. 6a have been reproduced by the model using a single set of parameters capable of reproducing the experimental data over the whole suction range and for different dry densities. Based on the calibration strategy presented by Della Vecchia et al. [9], the model parameters can be initially set to reproduce the retention curve corresponding to the sample with the highest density (ρ_{d} = 1.65 kg/m^3) and then, if necessary, adjusted to reproduce the water retention curves for the other dry densities. Remarkably, the model is able to reproduce, with a single set of five parameters, the main features of the role of dry density on the retention behavior of loess, i.e., the effect on the saturated water content of the material, the increase in AOV with void ratio and the almost negligible effect of dry density on water content at high suction values, as shown in Fig. 12. The model parameters used for the simulations are listed in Table 2.

To confirm the predictive capabilities of the model in reproducing the dry density effects, experimental data coming from Wang et al. [82] were also reproduced. The Authors prepared a compacted sample of loess coming

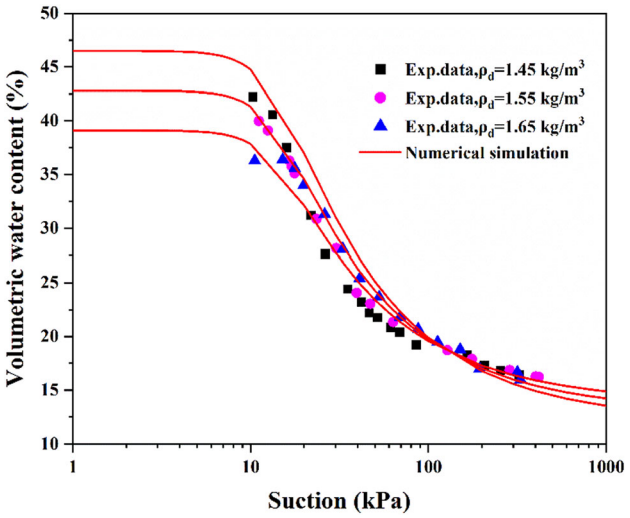

Fig. 12 Comparison of numerical modeling and experimental data (first wetting path) for the dry density effects of Yan'an loess. Experimental data are presented in Fig. 6a

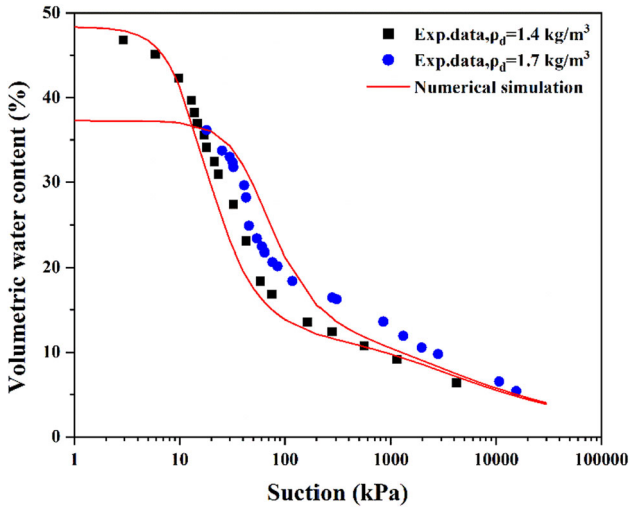

Fig. 13 Comparison of numerical modeling and experimental data for the dry density effects for the new district of Yan'an City loess (experimental data from Wang et al. [80])

Table 2 Water retention parameters for compacted loess

Location	Parameters				
	n_m	α_m (1/kPa)	n_M	m_M	α_1^M (kPa)
Yan'an City	1.4	$5.3*10^{-5}$	4	0.2	26
The new district of Yan'an City	1.3	$7.9*10^{-4}$	2	0.6	40

from the new district of Yan'an City, characterized by a liquid limit of 28.5% and a plastic limit of 18.7%. Five dry densities were considered, ranging from 1.40 to 1.80 kg/m^3. All samples were compacted at a water content of 10%. The compacted samples were then dried and finally subjected to a wetting process in order to measure the main wetting water retention curve of the material. The model predictions and parameters are shown in Fig. 13 and Table 2, respectively: For clarity, only two dry densities, 1.4 and 1.7 kg/m^3, are plotted in the figure. Again, the agreement between model predictions and experimental data is satisfactory, especially considering that the same set of material parameters was used to reproduce the water retention properties of the material over the density range. Again, calibration could be performed on the data corresponding to the highest density specimen and then the model parameters should be kept constant for the simulation of the specimen compacted at other densities. The numerical simulations are able to follow the slightly bimodal shape of the experimental water retention curve and correctly reproduce the intersection of the retention data, as well as the suction corresponding to the intersection of the curves, the increase in air-occlusion value with increasing dry density and the limited density effect in the high suction range. Model predictions and experimental results thus confirm that, even for compacted loess, the effects on the void ratio due to different compaction efforts are essentially related to a reduction in the size of macrovoids. Consistently, from the point of view of the retention curve, this mainly implies a change in the air-entry value of the material, as attested in the literature by Gallipoli et al. [19], Della Vecchia et al. [10] and Hadsari & Russel [24], among others. Furthermore, the low activity of the analyzed loess allows to neglect of the role of the evolving microstructure upon wetting (i.e., e_m is kept constant), which greatly simplifies the implementation of the water retention model and the number of material parameters required.

4.2 Wetting–drying cycles effects

When analyzing the water retention curves after wetting–drying cycles, it is clear that changes in the void ratio are not sufficient to interpret the evolution of the water retention properties. The comparison between Fig. 6a and Fig. 8a is paradigmatic: An increase in the compaction density implies an increase in the AOV of the water retention curves, as well as a crossing between them. Equation 16 has thus been considered as a state law capable of reproducing the effect of changes in inter-aggregate void ratio induced by mechanical loading and different compaction densities (as, e.g., [19, 74]), but if the change in material density is due to wetting–drying cycles and the associated irreversible fabric evolution described in

Sect. 3, a change in material parameters is required. This is reasonable and consistent with the different physical mechanisms induced by mechanical loading (i.e., affecting total volume changes) and wetting–drying cycles (i.e., mainly affecting the removal of soluble salts and cementitious materials). In particular, the effect on the formation of macropores due to the loss of soluble salts, which weakens the contact between particles during the wetting–drying cycles, has been reproduced at the phenomenological scale simply by changing the parameter α_1^M and keeping all other parameters fixed. This makes it possible to reproduce a different effect of changes in inter-aggregate porosity on the loess AOV when inter-particle contact is weakened. Figures 14a and 14b show the predictive capabilities of the model in terms of the evolution of the water

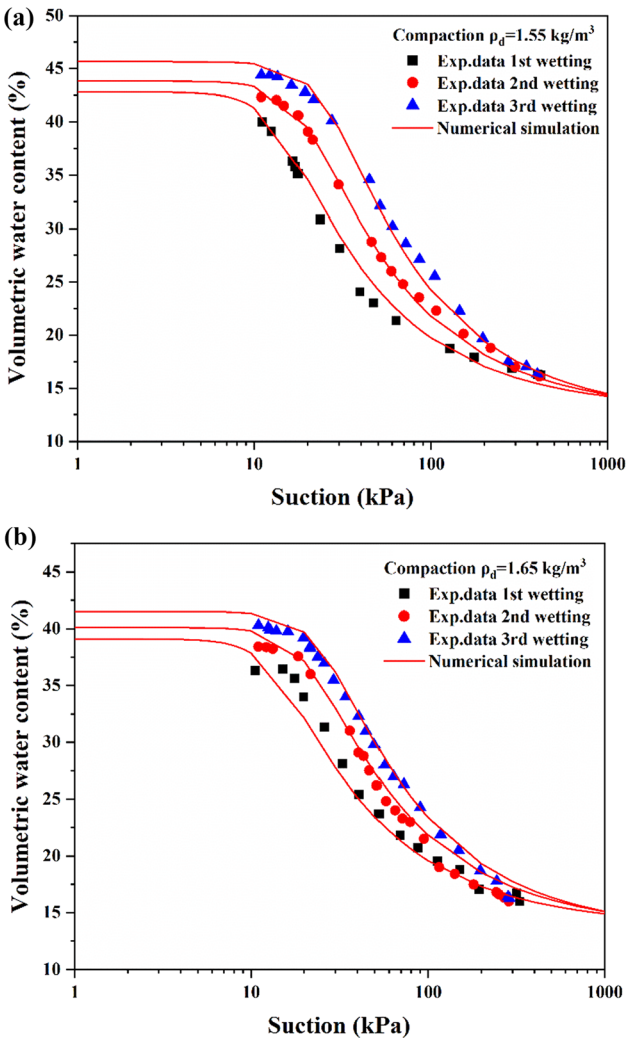

Fig. 14 **a** Comparison of numerical modeling and experimental data for the wetting–drying effects of Yan'an loess (experimental data presented in Fig. 7b). **b** Comparison of numerical modeling and experimental data for the wetting–drying effects of Yan'an loess (experimental data presented in Fig. 7c)

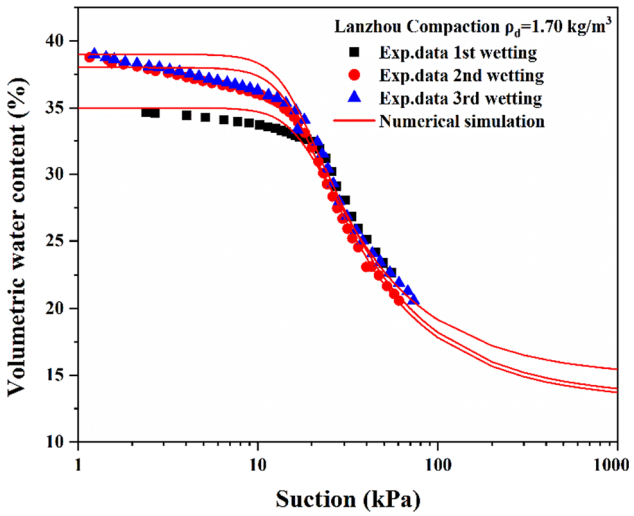

Fig. 15 Comparison of numerical modeling and experimental data for the wetting–drying effects for the Lanzhou City loess (experimental data presented in Zhao et al. [98])

retention properties of the material with increasing number of wetting–drying cycles, for two different compaction densities, namely 1.55 and 1.65 kg/m^3. The parameters used are the same as in Table 2, except for α_1^M, which takes the values 33 and 47 kPa for 2 and 3 cycles, respectively.

The experimental data of Zhao et al. [98] were also reproduced to demonstrate the predictive capability of the model in reproducing the effect of the wetting–drying cycle on compacted samples of loess coming from Lanzhou City, characterized by a liquid limit of 24.8% and a plastic limit of 15.5%. All samples were compacted at a water content of 12.3% and a dry density of 1.70 kg/m^3 and then subjected to 1, 2 and 3 wetting–drying cycles. The model simulations are shown in Fig. 15, while materials are listed in Table 3. It is worth noting that, in this case, all the parameters are kept the same regardless of the number of cycles. This further simplification with respect to the Yan'an loess has been possible because of the different particle size distributions: Loess from Lanzhou has a smaller particle size (only 1.2% of the particles are larger than 75 μm) compared to Yan'an loess (10.62% of the particles larger than 75 μm), so that the effect of particle rearrangement upon wetting–drying cycles is less relevant.

Table 3 Water retention parameters for Lanzhou compacted loess with different wetting–drying cycles

Parameters	n_m	α_m (1/kPa)	n_M	m_M	α_1^M (kPa)
	2	$7.9*10^{-5}$	4.5	0.2	24

5 Conclusions

In this paper, an experimental procedure using an EC-5 water sensor and an MPS-6 water potential was developed to measure the water retention curve of compacted loess samples prepared at different dry densities and subjected to different numbers of wetting–drying cycles. The water retention data were integrated with a detailed microstructural investigation, including morphological analysis (by scanning electron microscopy, SEM) and pore size distribution determination (by nuclear magnetic resonance, NMR). Despite the apparently unimodal shape of the water retention curve obtained at the phenomenological scale, the microstructural investigation provided evidence that compacted loess is characterized by a microstructure consisting of both intra-aggregate and inter-aggregate pores. In particular, the two classes of pores showed different responses to hydromechanical loading: According to the NMR data, the size of inter-aggregate pores tends to decrease with dry density and to increase with the number of wetting–drying cycles, whereas the size of intra-aggregate pores seems almost unaffected. In addition, the surface morphology information provided by the SEM images clarified that after three wetting–drying cycles, the structure of the compacted loess tends to become looser and larger inter-aggregate pores are formed due to the loss of soluble salts and cementing materials.

The ability to link the water retention curves obtained at the laboratory scale with the microstructural investigation allowed the development of a robust physically based double porosity theoretical framework for modeling the water retention behavior of compacted loess. The proposed model was developed following the framework presented by Della Vecchia et al. [9] for compacted clays. Accordingly, the water content of compacted loess was split into two contributions, one due to water belonging to intra-aggregate pores and one due to water stored in inter-aggregate pores. The proposed model requires only five parameters to capture the water retention properties of samples characterized by different compaction dry densities and subjected to different numbers of wet–dry cycles. Remarkably, a unique set of parameters is required to reproduce different water retention curves corresponding to different dry densities, which greatly simplifies the calibration procedure. The comparison between numerical simulations and experimental results, using both original data and data from the literature, shows that the increase in AOV with void ratio and the almost negligible effect of dry density on water content at high suction values are built in features of the model. Due to the different physicochemical mechanisms involved in the wetting and drying cycles, only one parameter is set to change to reproduce the influence of hydraulic cycles, as suggested by the microstructural interpretation.

In contrast to the modeling approaches presented in the literature, which often use ad hoc calibrations to account for density and wetting and drying cycle effects, the model presented encapsulates compacted loess within the broader conceptual framework of compacted geomaterials. On the other hand, many advanced water retention models have recently been presented in the literature, which are certainly able to reproduce several features of the water retention behavior of geomaterials (including the dependence on dry density, pore fluid composition, mechanical paths, etc.). However, these models are often characterized by a large number of parameters, some of which are difficult to calibrate using standard laboratory tests. In this context, the presented model represents a good compromise between simplicity and predictive capabilities, being on the one hand consistent with the microstructural features of loess, but on the other hand characterized by a limited number of material parameters, and thus easy to calibrate for engineering applications. Future investigations will focus on the response of the material to more than three wetting–drying cycles, assessing changes in both water retention properties and loess microstructure. Chemical analyses of the pore water would also provide useful complementary information. These data will ultimately help to evaluate the predictive capabilities of the retention model for a larger number of cycles, suggesting possible changes in the formulation to account for reaching steady-state conditions after a given number of wetting–drying cycles.

Acknowledgements The authors gratefully acknowledge the China Postdoctoral Science Foundation (Grant no. 2019T120873 and Grant no. 2018M631117), Postdoctoral Research Project in Shaanxi Province (Grant no. 2018BSHGZZHQYXMZZ26), the Key Program of the National Natural Science Foundation of China (Grant no. 41931285) and the key research and development program of Shaanxi Province (Grant no. 2019ZDLSF05-07).

Author contributions Wan-kui Ni, Gabriele Della Vecchia and Xiang-fei Lü designed research; Kang-Ze Yuan performed all experiments and analyzed the data; Yong-peng Nie, Hai-man Wang and Kang-ze Yuan calculated the pore distribution of loess samples. Kang-Ze Yuan and Gabriele Della Vecchia developed the model, performed the numerical simulation and wrote the paper. Gabriele Della Vecchia revised the manuscript. The map data in Fig. 1 was provided by the Data Center for Resources and Environmental Science, Chinese Academy of Science (RESDC) (http://www.resdc.cn). All authors read and approved the final manuscript.

Funding Open access funding provided by Politecnico di Milano within the CRUI-CARE Agreement.

Data availability Some or all data, models or codes that support the findings of this study are available from the corresponding author upon reasonable request. These include: numerical results of the simulations plotted in the paper; experimental data plotted in the

paper; numerical code for the implementation of the water retention model.

Declarations

Conflict of interest The authors declare no conflict of interest.

Ethical approval This article does not contain any studies with human participants and/or animals.

Informed consent Informed consent was obtained from all individual participants included in the study.

References

1. Assouline S, Tessier D, Bruand A (1998) A conceptual model of the soil water retention curve. Water Resour Res 34:223–231. https://doi.org/10.1029/97WR03039
2. ASTM (2006), Annual book of ASTM standards, ASTM international, West Conshohocken, PA
3. Bai X (1992) Microstructural deformation of clay. University of Glasgow
4. Bleam WF (1991) Soil science applications of nuclear magnetic resonance spectroscopy. Advances in agronomy. Elsevier, 91–155
5. Burton GJ, Pineda JA, Sheng D, Airey D (2015) Microstructural changes of an undisturbed, reconstituted and compacted high plasticity clay subjected to wetting and drying. Eng Geol 193:363–373. https://doi.org/10.1016/j.enggeo.2015.05.010
6. Costabel S, Yaramanci U (2013) Estimation of water retention parameters from nuclear magnetic resonance relaxation time distributions. Water Resour Res 49:2068–2079. https://doi.org/10.1002/wrcr.20207
7. Dathe A, Eins S, Niemeyer J, Gerold G (2001) The surface fractal dimension of the soil–pore interface as measured by image analysis. Geoderma 103:203–229. https://doi.org/10.1016/S0016-7061(01)00077-5
8. De la Morena G, Asensio L, Navarro V (2018) Intra-aggregate water content and void ratio model for MX-80 bentonites. Eng Geol 246:131–138. https://doi.org/10.1016/j.enggeo.2018.09.028
9. Della Vecchia G, Dieudonné AC, Jommi C, Charlier R (2015) Accounting for evolving pore size distribution in water retention models for compacted clays. Int J Numer Anal Meth Geomech 39:702–723. https://doi.org/10.1002/nag.2326
10. Della Vecchia G, Romero E (2013) A fully coupled elastic-plastic hydromechanical model for compacted soils accounting for clay activity. Int J Numer Anal Meth Geomech 37:503–535. https://doi.org/10.1002/nag.1116
11. Della Vecchia G, Scelsi G, Musso G (2019) Modeling the role of pore water salinity on the water retention behavior of compacted active clays. Riv Ital di Geotec (Ital Geotech J) 53(3):16–29
12. Dieudonné AC, Levasseur S, Charlier R, Della Vecchia G, Jommi C (2013) A water retention model for compacted clayey soils. Comput Geomech. https://doi.org/10.13140/RG.2.1.1707.5287
13. Dieudonné AC, Della Vecchia G, Charlier R (2017) Water retention model for compacted bentonites. Can Geotech J 54:915–925. https://doi.org/10.1139/cgj-2016-0297
14. Derbyshire E, Mellors TW (1988) Geological and geotechnical characteristics of some loess and loessic soils from China and Britain: a comparison. Eng Geol 25:135–175. https://doi.org/10.1016/0013-7952(88)90024-5
15. Fan X, Xu Q, Scaringi G et al (2017) A chemo-mechanical insight into the failure mechanism of frequently occurred landslides in the Loess Plateau, Gansu Province, China. Eng Geol 228:337–345. https://doi.org/10.1016/j.enggeo.2017.09.003
16. Feindel KW, Bergens SH, Wasylishen RE (2007) The influence of membrane electrode assembly water content on the performance of a polymer electrolyte membrane fuel cell as investigated by 1H NMR microscopy. Phys Chem Chem Phys 9:1850. https://doi.org/10.1039/b617551a
17. Gallage, Chaminda, Tehrani, Najmeh, Williams, David (2017) Instrumented large soil-column to investigate climate-induced ground deformation in expansive soil. In: Kim, D S (Ed.) Proceedings of the 19th international conference on soil mechanics and geotechnical engineering. International society for soil mechanics and geotechnical engineering, pp. 1147–1150
18. Gallegos DP, Smith DM (1988) A NMR technique for the analysis of pore structure: determination of continuous pore size distributions. J Colloid Interface Sci 122:143–153. https://doi.org/10.1016/0021-9797(88)90297-4
19. Gallipoli D, Wheeler SJ, Karstunen M (2003) Modeling the variation of degree of saturation in a deformable unsaturated soil. Géotechnique 53:105–112. https://doi.org/10.1680/geot.2003.53.1.105
20. Gao S, Chapman WG, House W (2009) Application of low field NMR T2 measurements to clathrate hydrates. J Magn Reson 197:208–212. https://doi.org/10.1016/j.jmr.2008.12.022
21. Genchi G, Sinicropi M, Carocci A et al (2017) Mercury Exposure and Heart Diseases. IJERPH 14:74. https://doi.org/10.3390/ijerph14010074
22. Gens A (2010) Soil–environment interactions in geotechnical engineering. Géotechnique 60:3–74. https://doi.org/10.1680/geot.9.P.109
23. Gu T, Wang J, Wang C et al (2019) Experimental study of the shear strength of soil from the Heifangtai Platform of the Loess Plateau of China. J Soils Sediments 19:3463–3475. https://doi.org/10.1007/s11368-019-02303-9
24. Hadsari V, Russell AR (2021) Pore-size evolution of a hydraulically deposited silty sand due to drying and rewetting. Géotechnique Letters 11:187–194. https://doi.org/10.1680/jgele.20.00147
25. Han Z, Vanapalli SK (2016) Stiffness and shear strength of unsaturated soils in relation to soil-water characteristic curve. Géotechnique 66:627–647. https://doi.org/10.1680/jgeot.15.P.104
26. Hou X, Qi S, Li T et al (2020) Microstructure and soil-water retention behavior of compacted and intact silt loess. Eng Geol 277:105814. https://doi.org/10.1016/j.enggeo.2020.105814
27. Howard JJ, Kenyon WE (1992) Determination of pore size distribution in sedimentary rocks by proton nuclear magnetic resonance. Mar Pet Geol 9:139–145. https://doi.org/10.1016/0264-8172(92)90086-T
28. Jiang M, Zhang F, Hu H et al (2014) Structural characterization of natural loess and remolded loess under triaxial tests. Eng Geol 181:249–260. https://doi.org/10.1016/j.enggeo.2014.07.021

29. Jin T, Cai X, Chen Y et al (2019) A fractal-based model for soil water characteristic curve over entire range of water content. Capillarity 2:66–75. https://doi.org/10.26804/capi.2019.04.02
30. Kleinberg RL, Flaum C, Griffin DD et al (2003) Deep sea NMR: methane hydrate growth habit in porous media and its relationship to hydraulic permeability, deposit accumulation, and submarine slope stability: DEEP SEA NMR. J Geophys Res. https://doi.org/10.1029/2003JB002389
31. Kleinberg RL (1994) Pore size distributions, pore coupling, and transverse relaxation spectra of porous rocks. Magn Reson Imaging 12:271–274. https://doi.org/10.1016/0730-725X(94)91534-2
32. Kleinberg RL (1996) Utility of NMR T2 distributions, connection with capillary pressure, clay effect, and determination of the surface relaxivity parameter ρ2. Magn Reson Imaging 14:761–767. https://doi.org/10.1016/S0730-725X(96)00161-0
33. Klukanova A, Sajgalik J (1994) Changes in loess fabric caused by collapse: an experimental study. Quatern Int 24:35–39. https://doi.org/10.1016/1040-6182(94)90036-1
34. Kohgo Y, Nakano M, Miyazaki T (1993) Theoretical aspects of constitutive modeling for unsaturated soils. Soils Found 33:49–63. https://doi.org/10.3208/sandf1972.33.4_49
35. Koliji A, Laloui L, Vulliet L (2010) Constitutive modeling of unsaturated aggregated soils: a constitutive model for aggregated soils. Int J Numer Anal Meth Geomech 34:1846–1876. https://doi.org/10.1002/nag.888
36. Kong LW, Tan LR (2000) A simple method of determining the soil-moisture characteristic curveindirectly. In: Rahardjo, H., Toll, D.G. Leong, E.C. (eds.), Unsaturated soils for Asia, Singapore, Balkema, Rotterdam, 341–345
37. Kong L, Sayem HMd, Tian H (2018) Influence of drying–wetting cycles on soil-water characteristic curve of undisturbed granite residual soils and microstructure mechanism by nuclear magnetic resonance (NMR) spin-spin relaxation time (T 2) relaxometry. Can Geotech J 55:208–216. https://doi.org/10.1139/cgj-2016-0614
38. Li H, Li T, Li P, Zhang Y (2020) Prediction of loess soil-water characteristic curve by mercury intrusion porosimetry. J Mt Sci 17:2203–2213. https://doi.org/10.1007/s11629-019-5929-2
39. Li XA, Li L, Song Y et al (2019) Characterization of the mechanisms underlying loess collapsibility for land-creation project in Shaanxi Province, China—a study from a micro perspective. Eng Geol 249:77–88. https://doi.org/10.1016/j.enggeo.2018.12.024
40. Li L, Li XA, Wang L et al (2020) The effects of soil shrinkage during centrifuge tests on SWCC and soil microstructure measurements. Bull Eng Geol Environ 79:3879–3895. https://doi.org/10.1007/s10064-020-01786-y
41. Li P, Li T, Vanapalli SK (2016) Influence of environmental factors on the wetting front depth: a case study in the Loess Plateau. Eng Geol 214:1–10. https://doi.org/10.1016/j.enggeo.2016.09.008
42. Li P, Vanapalli S, Li T (2016) Review of collapse triggering mechanism of collapsible soils due to wetting. J Rock Mech Geotech Eng 8:256–274. https://doi.org/10.1016/j.jrmge.2015.12.002
43. Li P, Xie W, Pak RYS, Vanapalli SK (2019) Microstructural evolution of loess soils from the Loess Plateau of China. CATENA 173:276–288. https://doi.org/10.1016/j.catena.2018.10.006
44. Li X, Hu C, Li F, Gao H (2020) Determining soil water characteristic curve of lime treated loess using multiscale structure fractal characteristic. Sci Rep 10:21569. https://doi.org/10.1038/s41598-020-78489-7
45. Li X, Zhang LM (2009) Characterization of dual-structure pore-size distribution of soil. Can Geotech J 46:129–141. https://doi.org/10.1139/T08-110
46. Liang C, Cao C, Wu S (2018) Hydraulic-mechanical properties of loess and its behavior when subjected to infiltration-induced wetting. Bull Eng Geol Environ 77:385–397. https://doi.org/10.1007/s10064-016-0943-x
47. Liu Z, Liu F, Ma F et al (2016) Collapsibility, composition, and microstructure of loess in China. Can Geotech J 53:673–686. https://doi.org/10.1139/cgj-2015-0285
48. Liu K, Ni WK, Li XT, Yuan KZ (2020) Indoor simulation test method for seepage and settlement deformation of fill foundation. Patent G01N3/12. 2020.
49. Loukidis D, Bardanis M, Lazarou G (2016) Classification, soil-water characteristic curve and swelling/collapse behavior of the Nicosia marl, Cypru. E3S Web Conf 9:11009. https://doi.org/10.1051/e3sconf/20160911009
50. Ma F, Yang J, Bai X (2017) Water sensitivity and microstructure of compacted loess. Trans Geotech 11:41–56. https://doi.org/10.1016/j.trgeo.2017.03.003
51. Monroy R, Zdravkovic L, Ridley A (2010) Evolution of microstructure in compacted London Clay during wetting and loading. Géotechnique 60:105–119. https://doi.org/10.1680/geot.8.P.125
52. Mu QY, Dong H, Liao HJ et al (2020) Water-retention curves of loess under wetting−drying cycles. Géotech Lett 10:135–140. https://doi.org/10.1680/jgele.19.00025
53. MUñOZ-CASTELBLANCO JA, Pereira JM, Delage P, Cui YJ, (2012) The water retention properties of a natural unsaturated loess from northern France. Géotechnique 62:95–106. https://doi.org/10.1680/geot.9.P.084
54. Musso G, Azizi A, Jommi C (2020) A microstructure-based elastoplastic model to describe the behavior of a compacted clayey silt in isotropic and triaxial compression. Can Geotech J 57:1025–1043. https://doi.org/10.1139/cgj-2019-0176
55. Navarro V, De la Morena G, Alonso J et al (2021) Numerical model of free swelling processes in compacted MX-80 bentonites. Int J Rock Mech Min Sci 141:104713. https://doi.org/10.1016/j.ijrmms.2021.104713
56. Ng CWW, Sadeghi H, Hossen SKB et al (2016) Water retention and volumetric characteristics of intact and re-compacted loess. Can Geotech J 53:1258–1269. https://doi.org/10.1139/cgj-2015-0364
57. Nuth M, Laloui L (2008) Advances in modeling hysteretic water retention curve in deformable soils. Comput Geotech 35:835–844. https://doi.org/10.1016/j.compgeo.2008.08.001
58. Olson KR (1985) Characterization of pore size distribution within soils by mercury intrusion and water –release methods. Soil Sci 139(5):400–404
59. Penumadu D, Dean J (2000) Compressibility effect in evaluating the pore-size distribution of kaolin clay using mercury intrusion porosimetry. Can Geotech J 37:393–405. https://doi.org/10.1139/t99-121
60. Prapaharan S, Altschaeffl AG, Dempsey BJ (1985) Moisture curve of compacted clay: mercury intrusion method. J Geotech Eng 111:1139–1143. https://doi.org/10.1061/(ASCE)0733-9410(1985)111:9(1139)
61. Pye K (1995) The nature, origin and accumulation of loess. Quatern Sci Rev 14:653–667. https://doi.org/10.1016/0277-3791(95)00047-X
62. Romero E, Della Vecchia G, Jommi C (2011) An insight into the water retention properties of compacted clayey soils. Géotechnique 61:313–328. https://doi.org/10.1680/geot.2011.61.4.313
63. Romero E, Gens A, Lloret A (1999) Water permeability, water retention and microstructure of unsaturated compacted Boom

clay. Eng Geol 54:117–127. https://doi.org/10.1016/S0013-7952(99)00067-8
64. Rost KT (2001) Late Holocene loess deposits and dust accumulation in the alpine meadow belt of the Wutai Shan, China. Quatern Int 76–77:85–92. https://doi.org/10.1016/S1040-6182(00)00092-6
65. Russ JC (1992) Characterizing and modeling fractal surfaces. J Comput Assisted Micro 4:73–126
66. Russell AR (2010) Water retention characteristics of soils with double porosity. Eur J Soil Sci 61:412–424. https://doi.org/10.1111/j.1365-2389.2010.01237.x
67. Russell AR (2014) How water retention in fractal soils depends on particle and pore sizes, shapes, volumes and surface areas. Géotechnique 64:379–390. https://doi.org/10.1680/geot.13.P.165
68. Sakaki T, Limsuwat A, Smits KM, Illangasekare TH (2008) Empirical two-point α -mixing model for calibrating the ECH2O EC-5 soil moisture sensor in sands. Water Resour Res. https://doi.org/10.1029/2008WR006870
69. Selig E, Ladd R (1978) Preparing test specimens using undercompaction. Geotech Test J 1:16. https://doi.org/10.1520/GTJ10364J
70. Smalley I, Rogers C (1996) Loess: the yellow earth. Geol Today 12:186–193. https://doi.org/10.1046/j.1365-2451.1996.00015.x
71. Strange JH, Rahman M, Smith EG (1993) Characterization of porous solids by NMR. Phys Rev Lett 71:3589–3591. https://doi.org/10.1103/PhysRevLett.71.3589
72. Tan Tjong Kie (1988) Fundamental properties of loess from Northwestern China. Eng Geol 25:103–122. https://doi.org/10.1016/0013-7952(88)90022-1
73. Tao G, Chen Y, Xiao H et al (2019) Determining soil-water characteristic curves from mercury intrusion porosimeter test data using fractal theory. Energies 12:752. https://doi.org/10.3390/en12040752
74. Tarantino A, De Col E (2008) Compaction behavior of clay. Géotechnique 58:199–213. https://doi.org/10.1680/geot.2008.58.3.199
75. Tian H, Wei C, Wei H et al (2014) An NMR-based analysis of soil-water characteristics. Appl Magn Reson 45:49–61. https://doi.org/10.1007/s00723-013-0496-0
76. Tovey NK (1971) Soil structure analysis using optical techniques on scanningelectron micrographs. In: Proceedings of 4th SEM symp. Chicago: IITResearch Institute
77. Vanapalli SK, Fredlund DG, Pufahl DE, Clifton AW (1996) Model for the prediction of shear strength with respect to soil suction. Can Geotech J 33:379–392. https://doi.org/10.1139/t96-060
78. Virtanen JK, Rissanen TH, Voutilainen S, Tuomainen T-P (2007) Mercury as a risk factor for cardiovascular diseases. J Nutr Biochem 18:75–85. https://doi.org/10.1016/j.jnutbio.2006.05.001
79. Walthert L, Schleppi P (2018) Equations to compensate for the temperature effect on readings from dielectric Decagon MPS-2 and MPS-6 water potential sensors in soils. J Plant Nutr Soil Sci 181:749–759. https://doi.org/10.1002/jpln.201700620
80. Wang H, Ni W, Yuan K et al (2021) Microstructure evolution of loess under multiple collapsibility based on nuclear magnetic resonance and scanning electron microscopy. J Mt Sci 18:2612–2625. https://doi.org/10.1007/s11629-021-6838-8
81. Wang JD, Li P, Ma Y et al (2020) Change in pore-size distribution of collapsible loess due to loading and inundating. Acta Geotech 15:1081–1094. https://doi.org/10.1007/s11440-019-00815-9
82. Wang Y, Li T, Li P et al (2021) Measurement and uniform formulation of soil-water characteristic curve for compacted loess soil with different dry densities. AdvCivil Eng 2021:1–9. https://doi.org/10.1155/2021/6689680
83. Wei Y, Fan W, Yu B et al (2020) Characterization and evolution of three-dimensional microstructure of Malan loess. CATENA 192:104585. https://doi.org/10.1016/j.catena.2020.104585
84. Wen T, Shao L, Guo X, Zhao Y (2020) Experimental investigations of the soil water retention curve under multiple drying–wetting cycles. Acta Geotech 15:3321–3326. https://doi.org/10.1007/s11440-020-00964-2
85. Xie W, Li P, Zhang M et al (2018) Collapse behavior and microstructural evolution of loess soils from the Loess Plateau of China. J Mt Sci 15:1642–1657. https://doi.org/10.1007/s11629-018-5006-2
86. Xie X, Li P, Hou X et al (2020) Microstructure of compacted loess and its influence on the soil-water characteristic curve. Adv Mater Sci Eng 2020:1–12. https://doi.org/10.1155/2020/3402607
87. Xu J, Li Y, Ren C, Lan W (2020) Damage of saline intact loess after dry-wet and its interpretation based on SEM and NMR. Soils Found 60:911–928. https://doi.org/10.1016/j.sandf.2020.06.006
88. Xu P, Zhang Q, Qian H, Qu W (2020) Effect of sodium chloride concentration on saturated permeability of remolded loess. Minerals 10:199. https://doi.org/10.3390/min10020199
89. Xu P, Zhang Q, Qian H et al (2021) Microstructure and permeability evolution of remolded loess with different dry densities under saturated seepage. Eng Geol 282:105875. https://doi.org/10.1016/j.enggeo.2020.105875
90. Ye Y, Zou W, Han Z, Liu X (2019) Predicting the entire soil-water characteristic curve using measurements within low suction range. J Mt Sci 16:1198–1214. https://doi.org/10.1007/s11629-018-5233-6
91. Yu B, Liu G, Liu Q et al (2019) Seasonal variation of deep soil moisture under different land uses on the semi-arid Loess Plateau of China. J Soils Sediments 19:1179–1189. https://doi.org/10.1007/s11368-018-2119-8
92. Yuan K, Ni W, Lü X et al (2022) Influence of wetting–drying cycles on the compression behavior of a compacted loess from microstructure analysis. Bull Eng Geol Environ 81:348. https://doi.org/10.1007/s10064-022-02854-1
93. Yuan K, Ni W, Lü X et al (2022) Mechanical properties and microstructure evolution of Malan loess. Quatern Int 637:74–84. https://doi.org/10.1016/j.quaint.2022.06.008
94. Zhai Q, Rahardjo H, Satyanaga A et al (2020) Estimation of the wetting scanning curves for sandy soils. Eng Geol 272:105635. https://doi.org/10.1016/j.enggeo.2020.105635
95. Zhang F, Cui YJ, Ye WM (2018) Distinguishing macro- and micro-pores for materials with different pore populations. Géotech Lett 8:102–110. https://doi.org/10.1680/jgele.17.00144
96. Zhang JW, Mu QY, Garg A et al (2020) Shear behavior of unsaturated intact and compacted loess: a comparison study. Environ Earth Sci 79:79. https://doi.org/10.1007/s12665-020-8820-0
97. Zhang L, Chen Q (2005) Predicting bimodal soil-water characteristic curves. J Geotech Geoenviron Eng 131:666–670. https://doi.org/10.1061/(ASCE)1090-0241(2005)131:5(666)
98. Zhao TY, Wang JF (2012) Soil-water characteristic curve for unsaturated loess soil considering density and wetting-drying cycle effects. Journal of Central South University (Science and Technology).43, 6